Broadband Ultrasonic Attenuation Estimation and Compensation With Passive Acoustic Mapping

Michael D. Gray and Constantin C. Coussios

***Abstract*— Several active and passive techniques have been developed to detect, localize, and quantify cavitation activity during therapeutic ultrasound procedures. Much of the prior cavitation monitoring research has been conducted using lossless *in vitro* systems or small animal models in which path attenuation effects were minimal. However, the performance of these techniques may be substantially degraded by attenuation between the internal therapeutic target and the external monitoring system. As a further step toward clinical application of passive acoustic mapping (PAM), this paper presents methods for attenuation estimation and compensation based on broadband cavitation data measured with a linear ultrasound array. Soft tissue phantom experiment results are used to illustrate: 1) the impact of realistic attenuation on PAM; 2) the possibility of estimating attenuation from cavitation data; 3) cavitation source energy estimation following attenuation compensation; and 4) the impact of sound speed uncertainty on PAM-related processing. Cavitation-based estimates of attenuation were within 1.5%–6.2% of the values found from conventional through-transmission measurements. Tissue phantom attenuation reduced the PAM energy estimate by an order of magnitude, but array data compensation using the cavitation-based attenuation spectrum enabled recovery of the PAM energy estimate to within 2.9%–5.9% of the values computed in the absence of the phantom. Sound speed uncertainties were found to modestly impact attenuation-compensated PAM energies, inducing errors no larger than 28% for a 40-m/s path-averaged speed error. Together, the results indicate the potential to significantly enhance the quantitative capabilities of PAM for ensuring therapeutic safety and efficacy.**

***Index Terms*— Array calibration, attenuation, cavitation, passive acoustic mapping (PAM), sound speed, ultrasound.**

I. Introduction

THE field of therapeutic ultrasound is now achieving clinical translation for applications ranging from neuromodulation [1] to ultrasound-mediated drug delivery across the blood–brain barrier [2] or to solid tumors [3], [4]. To reduce risk and improve treatment efficacy, several passive [5]–[10] and active [11]–[13] acoustic monitoring techniques have been developed, allowing localization and quantification of nonlinear acoustic emissions (including cavitation) from both targeted and off-target regions. Much of the passive acoustic mapping (PAM) algorithmic development and validation work reported to date has been conducted in lossless *in vitro* systems or small animal models in which soft tissue path attenuation effects were minimal. However, as with any extracorporeal ultrasound-based method, the performance of PAM techniques may be substantially degraded by attenuation between the internal therapeutic target and the external monitoring system. Nonetheless, studies conducted in larger animal models [14], [15] or *ex vivo* tissue [6], [16] have not quantified or corrected for attenuation effects.

Propagation through soft tissue may substantially alter the spectral content, size, and detectability of cavitation signals. By way of numerical example, a 5-MHz plane wave propagating through 4 cm of tissue with 0.5-dB/cm/MHz attenuation would undergo an order of magnitude energy loss. Moreover, since attenuation acts as a form of low-pass filter, the spatial resolution of images based on inertial (broadband) cavitation emissions may be considerably degraded. Estimation of unattenuated signal levels would be a critical step in relating absolute levels of cavitation activity to specific bioeffects which are sought or for which efficacy thresholds have been established [14], [16], [17].

Attenuation itself is an essential parameter in the planning of treatments such as high intensity focused ultrasound (HIFU) ablation or volumetric hyperthermia [18]–[20]. However, neither the spatial distribution nor the temporal variation [21]–[24] of this parameter is commonly known in clinical treatment scenarios.

Several methods for ultrasonic attenuation estimation have been developed based on backscatter data [25], [26], with transducer-related uncertainties reduced when using a reference phantom [27]. Since these techniques exploit ultrasound speckle patterns, they may be degraded when tissues of interest have low scattering density [28], [29], or when tissue sound speeds are not well known [30], [31]. Tomographic methods have also been developed [32], [33], allowing sound speed and attenuation mapping in human breast tissues using ring or conventional diagnostic arrays. These methods require through-transmission measurements or the existence of a planar reflector, respectively. They therefore do not appear well suited for application to larger (e.g., thoracic) volumes of common interest in therapeutic ultrasound.

As a further step toward clinical application of PAM, methods for understanding and mitigating the impacts of soft tissue attenuation are currently being developed. To address the need for a speckle-insensitive method that may be implemented with a single diagnostic array for any soft tissue

Manuscript received July 7, 2018; accepted August 15, 2018. Date of publication August 20, 2018; date of current version November 7, 2018. This work was supported by the National Institute for Health Research Oxford Biomedical Research Center. *(Corresponding author: Michael D. Gray.)*

M. D. Gray is with the Institute of Biomedical Engineering, University of Oxford, Oxford OX3 7DQ, U.K. (e-mail: michael.gray@eng.ox.ac.uk).

C. C. Coussios is with the Department of Engineering Science, Institute of Biomedical Engineering, University of Oxford, Oxford OX3 7DQ, U.K.

Digital Object Identifier 10.1109/TUFFC.2018.2866171

not encased in bone (i.e., nonintracranial), an attenuation estimation technique based on broadband cavitation emissions is presented. A set of soft tissue phantom experiments is used to illustrate: 1) the impact of attenuation on PAM images; 2) the estimation of attenuation from cavitation data; 3) image recovery following attenuation compensation of PAM input data; and 4) the impact of sound speed uncertainty on baseline PAM processing, attenuation estimation, and image recovery. The proposed techniques may allow restoration of PAM energy estimation and resolution, improved treatment monitoring and guidance, and mapping of tissue attenuation over the course of a treatment all without additional measurements or resources.

The passive and active cavitation imaging methods cited above all are intended to ultimately improve upon the current clinical practice of bubble detection through relative echo enhancement of B-mode images acquired between HIFU transmissions. This emerging class of methods allows detection and mapping of bubble activity while revealing additional information that relates to therapeutic effects (e.g., spectral features denoting types of bubble behavior, or total cavitation dose). In the particular case of passive methods, by estimating and compensating for actual tissue attenuation, the real-time monitoring of bubble activity during HIFU transmissions would be minimally impacted by patient-to-patient variability. Critically, this would allow absolute or at least consistent quantitative assessments of cavitation emissions and their relationship to independently observed bioeffects. Moreover, when sharing an array used for conventional diagnostic ultrasound, PAM is automatically coregistered with the B-mode image, allowing enhanced treatment guidance by showing cavitation events superimposed on patient tissue morphology. In the absence of any other techniques capable of achieving these benefits during therapeutic ultrasound exposure, PAM is expected to play a major role in clinical treatment monitoring.

II. Methods

This section begins with a summary of the PAM beamforming algorithms employed in the present study, in order to clarify the assumptions made and data required. This is followed by a description of the array characterization procedures that are intended to provide calibrated data to the PAM beamformers. Next, descriptions are provided of the cavitation measurements that were used to generate PAM algorithm input data in lossless and attenuating media. The section concludes with procedures used for cavitation-based attenuation estimation and compensation of PAM input data.

A. PAM Algorithms

In the present work, cavitation emissions received with conventional ultrasound linear arrays were processed with two PAM algorithms that have been adopted for cavitation monitoring: time exposure acoustics (TEA) [34] and robust Capon beamforming (RCB) [8]. The former provides a computationally simple method of mapping sources of cavitation at the expense of spatial resolution, while the latter provides superior spatial resolution but at considerable computational cost. These two algorithms are thought to bracket the resolution capabilities of known passive mapping algorithms published to date. Both algorithms operate on time domain calibrated array response signals $p(t, \boldsymbol{r}_j)$ received at array element locations $\boldsymbol{r}_j$ for time duration T to produce an estimate of monopolar source energy $E(\boldsymbol{r})$ at an observation location $\boldsymbol{r}$

$$E(\boldsymbol{r}) = \frac{1}{4\pi\rho c}\int_{t_0}^{t_0+T} q^2(\boldsymbol{r}, t)dt \tag{1}$$

where ρ and c are the density and sound speed of the ambient medium, respectively, t_0 is the start time of the data record, and bold type quantities indicate vectors. The source strength q as a function of time t is defined by a sum over the $j = 1:J$ array elements

$$q(\boldsymbol{r}, t) = \frac{1}{J}\sum_{j=1}^{J} 4\pi\, w_j |\boldsymbol{r}_s|\, p(\boldsymbol{r}_j, t+|\boldsymbol{r}_s|/c) \tag{2}$$

where $\boldsymbol{r}_s = \boldsymbol{r}_j - \boldsymbol{r}$, $||$ is the magnitude of the enclosed argument, and w_j are the weights applied to each element. All weights in the TEA beamformer are set to unity, while RCB optimizes the weights for each imaging location $\boldsymbol{r}$ in order to minimize the variance of the array output, with allowance for uncertainties in array element sensitivity and location [35]. Control over the degree to which weights may be adjusted is provided by a single input factor ϵ. Previous work [8] has shown that ϵ values in the range of 1–10 may yield acceptable results with an uncalibrated array. From a preliminary review of the present data sets, it appeared that RCB performed well with ϵ values near unity once the array elements were calibrated. Therefore, a fixed value of $\epsilon = 1$ was used in this study. The time window $t_0 \le t \le (t_0 + T)$ contains cavitation signals generated by pulsed ultrasound of duration $\sim$0.8$\times$T, so that (1) is an estimate of the source energy associated with a finite sequence of events. Energy maps were generated in a 2-D (depth, azimuth) grid in the zero-elevation plane.

For accurate estimation of source energy, the array signals in (2) must account for both element directivity and propagation path attenuation [9]. Specifically for the former, the delay and amplitude scaling operations with respect to the distance between the element and imaging locations ($|\boldsymbol{r}_s|$) in (2) presume a point (omnidirectional) model for signal reception. In actuality, both the finite-array element size and the overlying lens may significantly modify the characteristics of the received signals [36], [37].

In the present work, the raw array voltage signals $v_j(t)$ acquired as a function of time t during a cavitation monitoring experiment contain three response-biasing effects

$$v_j(t) = p_j(t) \otimes M_j(t) \otimes D_j(t, \boldsymbol{r}_s) \otimes A_j(t, \boldsymbol{r}_s) \tag{3}$$

where $M_j(t)$, $D_j(t, \boldsymbol{r}_s)$, and $A_j(t, \boldsymbol{r}_s)$ represent element sensitivity, diffraction, and path attenuation and ($\otimes$) represents a time domain convolution. The diffraction term captures directivity effects that vary with the relative position of array element and source [38], while the electroacoustic sensitivity terms are element specific but source independent.

For simplicity of practice, the deconvolution of electroacoustic and path propagation effects described in (3) is

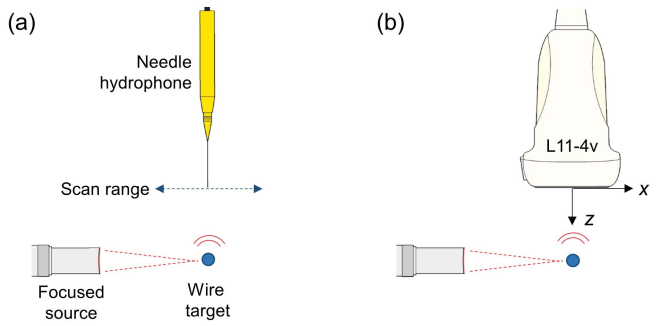

Fig. 1. Array characterization measurements. (a) Wire scattering pressure field mapping. (b) Substitution calibration for an L11-4v array. Objects and distances are not drawn to scale.

performed in the frequency domain

$$p_{0,j}(f) = V_j(f)/(M_j(f) \times D_j(f, \boldsymbol{r}_s) \times A_j(f, \boldsymbol{r}_s)) = p_{a,j}(f)/A_j(f, \boldsymbol{r}_s) \quad (4)$$

where $p_{a,j}(f) = V_j(f)/H_{\text{cal},j}(f, \boldsymbol{r}_s)$ is the calibrated array response (uncorrected for attenuation) and $H_{\text{cal},j}(f, \boldsymbol{r}_s) = M_j(f) \times D_j(f, \boldsymbol{r}_s)$ is the array calibration for sensitivity and diffraction. Procedures for determination of the calibration terms in (4) are presented in Sections II-B and II-E.

B. Array Characterization

1) Arrays and Data Collection: The present study employed a pair of L11-4v arrays (Verasonics, Kirkland, WA, USA), each having 128 elements with 0.30-mm spacing. Data from the arrays were collected using a 256-channel configurable ultrasound array controller (Vantage 256, Verasonics), which was also used to provide synchronization pulses to auxiliary data collection equipment. The L11-4v arrays were calibrated using a method for simultaneous quantification of sensitivity and diffraction effects. All experiments were conducted in a tank filled with filtered and degassed water, and all data were processed in MATLAB (Mathworks, Natick, MA, USA).

2) Element Sensitivities and Diffraction: The combined element sensitivity and diffraction responses $H_{\text{cal},j}(f, \boldsymbol{r}_s)$ for the L11-4v arrays were found using a calibrated scattering experiment (Fig. 1). The scattering target consisted of a 10-cm length of a 0.10-mm diameter Tungsten wire (Goodfellow Cambridge Limited, Huntington, U.K.) held taut in a clear plastic fixture (not shown). The acoustic field to be used as a calibration reference was formed by irradiating the wire at the focus of a broadband (4–11 MHz) transducer with a 1.2-mm full width half power beam at 7.5 MHz (V320-SU, 0.5″ diameter, 75-mm focus, Olympus NDT, Essex, U.K.). The use of a focused source and small diameter wire was intended to cumulatively minimize the directivity of the scattered field. The source was driven with a pulser (5072PR, Olympus NDT), and the scattered field was characterized using a needle hydrophone (75-μm diameter, Precision Acoustics, Dorchester, U.K.) whose calibration $M_{\text{hyd}}(f, \theta)$ had previously been determined as a function of incidence angle [38].

Hydrophone signals were preamplified (50 dB) using the receiver stage of the pulser prior to oscilloscope data acquisition (HDO 4024, LeCroy, Geneva, Switzerland) in order to make the best use of digitizer dynamic range. The preamplification gain and phase transfer function $G_{\text{pre}}(f)$ was determined as a function of frequency using a reference signal provided by a waveform generator (single 8-MHz cycle with usable bandwidth of 2–15 MHz, from model 33250A, Agilent Technologies, Cheshire, U.K.) and calculating the spectral ratio of amplified and unamplified signals. Hydrophone positioning and oscilloscope data collection were coordinated by control software (UMS3, Precision Acoustics) and synchronized by a trigger from the pulser.

The wire scattered field was characterized by scanning the hydrophone over a 40-mm line (encompassing the 38.4-mm receive aperture of the arrays) at z-offsets of 35, 45, and 55 mm. Supplemental ± 3 mm y-axis scans (covering the 4-mm elevation aperture of the array elements) were conducted at the center of each 40-mm line in order to quantify any directivity of the wire scattering that may ultimately affect elevational integration by the array elements. Range estimates were based primarily on propagation time found from a temperature-sound speed relation for water [39], but also included corrections for an observed trigger to transmission delay, and the delay through the external hydrophone preamplifier. In order to improve measurement signal-to-noise ratio (SNR), the signal at each scan point was averaged four hundred times on the oscilloscope prior to storage.

After completing the field characterization measurements, the L11-4v arrays were installed in turn, and their responses were measured at the same nominal z-offsets as scanned with the hydrophone, as independently confirmed using B-mode imaging of the wire. Pulser output and array signal reception were coordinated with a trigger from the array controller.

To create a calibrated reference field $p_{\text{hyd}}(f, x, z)$, hydrophone voltage signals were processed according to the following steps: 1) application of a third-order 200-kHz high-pass Butterworth filter for low-frequency noise removal; 2) application of a 20% Tukey window to exclude direct path signals from the focused source and reduce endpoint artifacts in subsequent frequency processing; 3) calculation of Fourier transforms $X(f, x, z)$ for each field point; and 4) correction for sensitivity, directivity, and preamp gain $G_{\text{pre}}(f)$ according to

$$p_{\text{hyd}}(f, x, z) = B(f, z)X(f, x, z)/(M_{\text{hyd}}(f, x, z)G_{\text{pre}}(f)) \quad (5)$$

where the hydrophone sensitivity $M_{\text{hyd}}(f, x, z)$ at each field point was interpolated from the angular hydrophone directivity $M_{\text{hyd}}(f, \theta)$ using $\theta = \tan(x/z)$, and $B(f, z)$ is a dimensionless elevation directivity correction found from the spatially averaged hydrophone output along the elevation direction (y) normalized by the response at zero elevation.

Array element calibrations $H_{\text{cal},j}(f, 0, z)$ were calculated at each depth by filtering and windowing the raw array voltage signals $V_j(f, 0, z)$ as with the hydrophone data, and

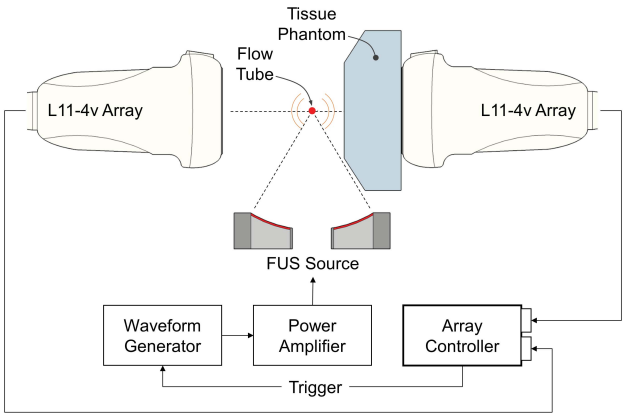

Fig. 2. Cavitation experiment configuration. Cavitation signals were produced by using a focused source to excite SonoVue flowing through a small tube oriented normal to the page. A pair of arrays simultaneously monitored ultrasonic emissions from the tube through two distinct paths: one consisting only of water, and the other containing an attenuating soft tissue phantom. The transducers, flow tube, and phantom were fully submerged in degassed water.

normalizing by the calibrated reference field

$$H_{\text{cal},j}(f,0,z) = V_j(f,0,z)/p_{\text{hyd}}(f,x_j,z) \tag{6}$$

where p_{hyd} was linearly interpolated from the scan line positions x to the presumed array element positions x_j. Since the reference field contains absolute pressure as a function of position, (6) provides a combined array element calibration for electroacoustic sensitivity and diffraction in the $x-z$ plane for a source on the z-axis ($x = y = 0$). Procedures for application of these calibrations to array observations of cavitation are described in Section II-C2.

C. Cavitation Experiments

1) Test Configuration: In order to determine the effect of attenuation on PAM performance and assess the ability to estimate and compensate for attenuation, experiments were conducted by using the pair of notionally identical L11-4v arrays to simultaneously monitor cavitation generated inside a tube containing a flowing ultrasound contrast agent (UCA) (Fig. 2). This configuration allowed for direct comparison of cavitation events viewed through water and through an attenuating soft tissue phantom. The components and conduct of these experiments are described below. All experiments were conducted inside a tank filled with filtered and degassed water at temperatures between 19 °C and 21 °C.

A single-element focused ultrasound (FUS) transducer was employed as a source for cavitation generation. The transducer had a fundamental frequency of 1.06 MHz, a 64-mm active diameter, and a 62.6-mm spherical geometric focus (H102, Sonic Concepts, Woodinville, WA, USA). A 30-cycle tone burst drive signal was provided by a waveform generator (model 33250A, Agilent Technologies), passed on to a power amplifier (model 1040L, Electronics and Innovation Ltd., Rochester, NY, USA) and then on to a matching transformer and the transducer itself.

The source transducer was directed at a 0.3-mm inner diameter, 0.6-mm outer diameter polyethylene tube (SIMS Portex Ltd., Hythe, U.K.) through which a UCA (SonoVue, Bracco, Milan, Italy) flowed. A 10-cm length of tube was held vertically in a C-shaped Perspex holder mounted on a three axis Cartesian positioning system (PRO-115, Aerotech, Hampshire, U.K.). The holder location was set so that the tube center was aligned with the source main lobe, and so that holder scattering would be minimized. The UCA was diluted 50% by volume with filtered water, placed in a 5-mL syringe, and driven with a syringe pump (AL-1000, World Precision Instruments, Sarasota, FL, USA) to provide a flow rate of 0.1 mL/min. Before each experiment, the syringe was removed from the pump and lightly shaken and rotated in order to remix the UCA suspension.

Sound scattering from the flowing UCA and its containing tube was monitored with two L11-4v arrays, with the array controller providing data acquisition, conventional diagnostic imaging, and real-time PAM implementation. The arrays were installed on three-axis manual positioners and configured for coaxial and coplanar alignment. This was confirmed prior to tube installation by B-mode imaging with each array of a 3.1-mm-diameter stainless steel spherical target suspended on a 0.3-diameter stainless wire. Array positions were manipulated so that the target appeared at the same location in the B-mode image (within 0.25 mm) and with maximum image strength. Azimuthal co-planarity was further confirmed with a mechanical level. Finally, the sphere target was removed and replaced by the UCA tube system. In this configuration, the position of the tube was centered between the stationary arrays, again under B-mode guidance.

The FUS drive level was chosen to be the approximate minimum that consistently produced inertial cavitation, as determined by the presence of elevated broadband noise during real time review of the array channel spectra observed with a custom MATLAB script running on the array controller. Cavitation signals were monitored with the linear arrays during source transmissions, with all system timing coordinated by a synchronization pulse emitted once per second from the array controller. Array time-series data were acquired for a total of 200 μs (sufficient to capture the cavitation data bounded by 60+ μs duration signal-free windows), digitized with 14 bits at 25 MHz without any spectral shaping except for that which was provided by the controller's antialiasing filters, and stored for subsequent analysis. The largest of the time domain cavitation signals used 9–10 bits of the 14-bit dynamic range, so digitizer input saturation was of no concern.

For introduction of attenuation into the experiment, a soft tissue phantom material [40] was chosen for its realistic sound speed, attenuation, and scattering properties. To prepare the phantom, the agar-based material was mixed and poured into a cuboid mold and cut after 24 hours of refrigerated curing to a final size of $10 \times 4 \times 3$ cm^3. Corners were removed in order to minimize perturbation of the FUS field (Fig. 2). During cavitation experiments, the phantom block was placed between the flow tube and one of the arrays, with the block in contact with the array lens.

2) Array Data Processing: The acquired time series in all cavitation experiments contained three segments: 1) an initial signal-free window; 2) the cavitation signal; and 3) noise prior to arrival of scattering from experiment rigging. An initial window of no less than 60 μs consisting solely of background noise was used for calculation of SNR for each array element. The duration of the time series that exhibited cavitation behavior (broadband noise elevation) was the same as the duration of the source drive pulse (27.3 μs).

Individual element corrections were applied to raw array cavitation monitoring data in the frequency domain. Processing steps consisted of 1) application of a 20% Tukey window to the time domain array data $v_j(t)$ in order to capture cavitation events and minimize the cumulative level of electronic noise; 2) calculation of windowed array data Fourier transforms $[V_j(f)]$; and 3) application of sensitivity and diffraction correction terms $H_{\text{cal},j}(f, \boldsymbol{r}_s)$ as in (4). Since the diffraction portion of the calibration is dependent on source position, (4) was only evaluated at the restricted range of source and corresponding calibration locations described in Section II-B2.

D. Tissue Phantom Characterization

For comparison with cavitation-based attenuation estimates, the soft tissue mimicking phantom was characterized using conventional through-transmission measurements made with a single-element unfocused source (Panametrics V309, 5 MHz, 12.7 mm diameter, Olympus NDT) and a needle hydrophone (200 μm, Precision Acoustics). The unfocused source was driven with a pulser (5072PR, Olympus NDT) and moved to three locations along each phantom to obtain independent property estimates. At each of these locations, the hydrophone was scanned over a small 2-D area (1.2×1.2 mm^2, 0.2-mm steps) parallel to the source face in order to check for refraction due to misalignment, and to allow subsequent spatial integration. Hydrophone signals were preamplified (SR445A, Stanford Research Systems, Palo Alto, CA, USA) before oscilloscope digitization (Waverunner 64Xi, LeCroy). Data sets were acquired with and without the phantom in the propagation path and were used together to estimate sound speed and attenuation using conventional processing methods as follows.

Speed of sound was determined from the propagation time difference (Δt) measured with and without the phantom installed [41]

$$c_{\text{thru}}(f) = c_w(1 + c_w \Delta t / h)^{-1} \tag{7}$$

where c_w is the speed of sound in water at the recorded temperature [39] and h is the thickness of the phantom (2.95 cm $\pm$ 0.01). The frequency dependence was assessed by conditioning the time domain data with a series of second-order Butterworth bandpass filters with 1-MHz bandwidth centered at frequencies f: 3.6:0.5:9.1 MHz and evaluating (7) in each passband.

Attenuation (np/cm) was estimated from unfiltered Fourier transforms of the data recorded with (X_{phan}) and without (X_{water}) the phantom, using

$$\alpha_{\text{thru}}(f) = -\ln(|X_{\text{phan}}/X_{\text{water}}|)/h \tag{8}$$

where ln( ) indicates natural logarithm. Effects of sample surface reflection on the attenuation measurement were considered negligible based on the sound speed and density of the material.

All phantom characterization measurements were conducted on the same day and in the same water tank as the cavitation experiments in order to maximize consistency of phantom temperature and age. Density was subsequently determined using a mass scale and the phantom dimensions, and was used for estimation of the transmission coefficient.

E. Attenuation Estimation

Inertial cavitation events radiate a broad spectrum of noise as a consequence of their temporally impulsive nature [42]. Limited bandwidth observations of spectrally flat cavitation emissions in low-loss media have been reported using calibrated instrumentation [43]–[45]. In a clinical therapeutic ultrasound context, the cavitation spectrum would be modified relative to that which is observed in a lossless homogeneous medium by the cumulative attenuation through the constituent soft tissues between the internal bubble and the external measurement location. Signal level losses may be compounded by refraction (modifying path length) and tissue interface reflection/transmission, although the latter should be independent of frequency for many soft tissue treatment scenarios of interest. Specifically, the propagation media are weakly dispersive and impedance mismatches are small enough so that layered tissue resonance effects are negligible.

In a homogeneous attenuating medium, the cavitation spectrum is modified simply by $e^{-\alpha|\boldsymbol{r}_s|}$, where α is the attenuation and $|\boldsymbol{r}_s|$ is the path length. In principle, if the location of a cavitation source is known, α can be estimated directly from the spectrum shape. In the present work, source location is estimated from PAM processing, and attenuation is found from a functional fit to the calibrated broadband cavitation emission spectrum. Application of this approach to a system with multiple propagation media provides an estimate of path-averaged attenuation.

The procedural steps for attenuation estimation using broadband cavitation emissions are illustrated in Fig. 3. Cavitation is monitored with an array whose data are calibrated according to the preceding sections and fed to a PAM algorithm for detection and mapping of broadband emissions. Cavitation source location is estimated from isointensity contours surrounding the map peak [46]. This approach is intended to resolve ambiguities due to the existence of multiple closely spaced sources and confounding influences of beamformer sidelobes and noise. Contour levels were set in 10% decrements relative to the map peak level, and an equivalent source position is found from

$$x_{\text{eq}} = \frac{1}{MN}\sum_{m=1}^{M}\sum_{n=1}^{N} C_{mn}(x) \tag{9a}$$

$$z_{\text{eq}} = \frac{1}{MN}\sum_{m=1}^{M}\sum_{n=1}^{N} C_{mn}(z) \tag{9b}$$

$$|\boldsymbol{r}_{\text{eq}}| = \left(x_{\text{eq}}^2 + z_{\text{eq}}^2\right)^{1/2} \tag{9c}$$

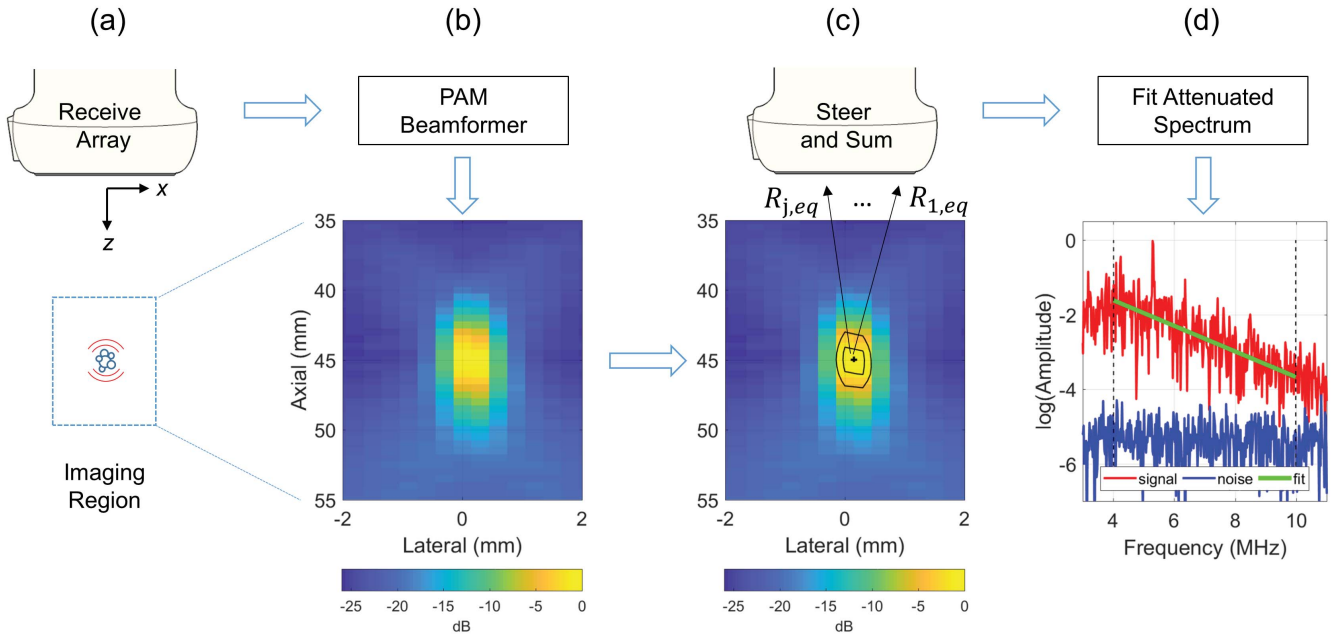

Fig. 3. Attenuation estimation process. (a) Cavitation monitoring with an array, shown here as but not required to be a conventional linear array. (b) Array data are processed with a PAM beamforming algorithm to detect and map cavitation activity. (c) Map data are used to estimate emission source location (which may be between imaging points). Array data are then steered to the estimated source location, summed, and Fourier transformed. (d) The resulting spectrum is fit to an exponential function within a frequency range determined by SNR and calibration bandwidth.

where x_{eq} and z_{eq} are the source lateral and depth coordinates and C_{mn} are the M isointensity contours (typically $M = 3$) consisting of N points.

Once an equivalent source position has been found, the array is steered to that position assuming spherical spreading, and the calibrated spectra are summed

$$s(f) = \sum_{j=1}^{J} p_{a,j}(f) \times (R_{s,\text{eq}} e^{ikR_{s,\text{eq}}}) \tag{10}$$

where $R_{s,\text{eq}} = |\boldsymbol{r}_j - \boldsymbol{r}_{\text{eq}}|$ and $k = 2\pi f/c$. Since the beamformers are evaluated at a series of independent field points which have no inherent area or volume, spherical spreading between each imaging point and each array receiver is appropriate provided that the directivity associated with the finite-array element size has been compensated for [as in (4)]. An equivalent calculation is performed on background noise acquired during PAM data collection, so that a steered noise estimate $nz(f)$ can be used to define the steered SNR: $\text{SNR}(f) = |s(f)/\text{nz}(f)|$. This quantity is used to define the highest frequency retained for the attenuation estimation process, with the threshold value typically set to 2 (see Section III-C). The lower frequency bound is typically limited by the availability of array calibration data (3.6 MHz).

The path-averaged attenuation is found by fitting the steered spectrum to an exponential of the form $A\exp(-bf_u^m)$, where A, b, and m are constants to be determined in the fitting process and f_u is the frequency band defined by the SNR of the beamformed spectra (upper bound) and calibration constraints (lower bound). The fitting process is numerically better behaved in logarithmic space, so $\ln(s(f_u))$ was fit with $\ln(A\exp(-bf_u^m))$ using the fit function in MATLAB. The power law expression provides an estimate of total path attenuation

$$\bar{\alpha}_{\text{est,tot}}(f) = b \times f^m \tag{11a}$$

and the path-average attenuation per unit distance is given by

$$\alpha_{\text{est,avg}}(f) = (b/\langle R_{s,\text{eq}} \rangle) \times f^m \tag{11b}$$

where $\langle\,\rangle$ indicates the average over the array elements. The total attenuation in (11a) has units of nepers (np), while the average attenuation per unit distance in (11b) typically is processed with units of np/cm. Note that in this proposed approach, attenuation is determined by spectrum shape, and not by absolute signal size.

F. Attenuation Compensation

The attenuation obtained from (11a) may be used to estimate the cavitation source energy distribution that would have been observed in a nonattenuating medium. In a clinical setting, doing so would allow absolute comparison of cavitation activity among measurements made at different depths and different constituent tissues in the propagation path. The process begins by compensating the individual calibrated array channel data $p_{a,j}(f)$ [see (4)] for attenuation in the frequency domain

$$p_{0,j}(f) = p_{a,j}(f) \times e^{\bar{\alpha}_{\text{est,tot}}(f)}. \tag{12}$$

Array element SNR tends to drop with increasing frequency as a consequence of element diffraction and path attenuation, and care must be taken not to excessively enhance high-frequency noise when deconvolving the factors that limit the high-frequency response (electroacoustic response, diffraction, and attenuation). All array elements are therefore

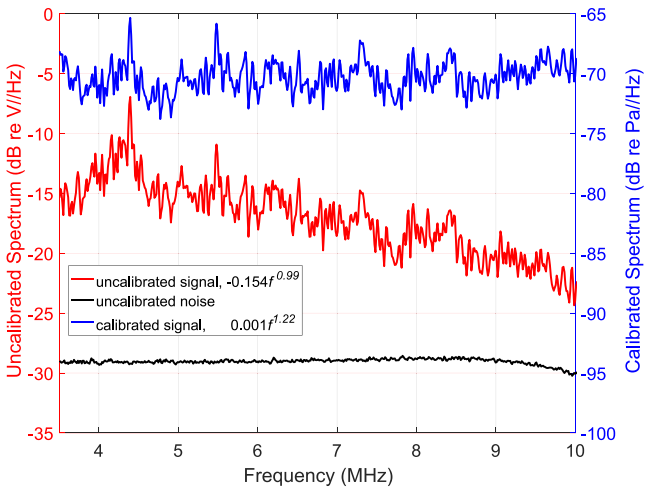

Fig. 4. Calibration demonstration using element and shot averaged responses during the tube flow experiment on the array with a water propagation path. Expressions in the legend are power law fits between 3.6 and 9.5 MHz, where the calibration ($H_{\text{cal},j}$) SNR was at least 10 (linear) for all array elements. Uncalibrated signal (red curve) and noise (black curve) are quantified on the left ordinate, while the calibrated spectrum is quantified on the right ordinate.

conditioned with a bandpass filter whose low-pass corner f_L is the array-averaged frequency at which each element crossed the SNR threshold used in attenuation processing ($\langle f_{L,j}\rangle$), and the high-pass corner frequency f_H is set to the minimum of f_u. As a further signal quality safeguard, only channels with a suitable minimum of useable bandwidth ($f_{L,j} - f_H \geq \Delta f$) are passed to the PAM beamformer. For the broadband signal analysis in the present study, a minimum sensor analysis bandwidth of $\Delta f = 2$ MHz was used. Bandpass filter coefficients were calculated using a fifth-order Butterworth formulation, and the final calibrated and attenuation compensated time domain signals are found from

$$p_{0j}(t) = B_0\{\text{Re}[\text{IFT}(p_{0,j}(f))]\} \tag{13}$$

where IFT indicates an inverse Fourier transform, Re[ ] indicates the real part of the argument in braces, and $B_0\{\}$ indicates a bandpass operation with corner frequencies determined as above, with signals run through the filter both forward and backward in order to remove passband phase distortion. The pressures in (13) are used with the expressions in (2) and (1) to yield estimates of monopolar source energy in the absence of any attenuation in the propagation path.

It is important to emphasize at this stage that the water path array is not used in any way for estimation of attenuation. Its role is for analyses of the proposed methods, serving as a basis of comparison with the attenuated path array response before compensation, and for validation of attenuation compensation processing.

III. Results

A. Calibrated Array Signals

An example of the effect of sensitivity and diffraction calibration on cavitation signals recorded during the cavitation experiment is shown in Fig. 4 for one array prior to installation of the attenuating phantom. The uncalibrated (red) and calibrated (blue) signal curves were calculated from spectrum magnitude averages over all array elements and over 20 consecutive FUS pulse exposures ("shots"). In the absence of calibration, the data show a complex spectral shape with a broadband trend to decrease with increasing frequency. The legend entry shows the power law fit to the spectrum, illustrating how the uncalibrated array response could be mistaken for a substantial excess path attenuation. By comparison, the calibrated result has a relatively flat broadband spectral trend, enabling the use of calibrated data from a single array for subsequent attenuation tests and analyses.

Harmonic scattering is visible in this data set, most notably at 4 and 5 times the FUS fundamental frequency. Narrow band spectral features can interfere with the proposed fitting process (11), especially when overall data bandwidth is limited by SNR. Therefore, in subsequent sections, attenuation estimation results will be compared both with the data as-is, and with a notch filter applied. The low-pass characteristics of element sensitivity and diffraction responses limit the useable upper frequency range of the data. The highest frequency used in these data sets was limited to 9.5 MHz based on calibration SNR (see Section II-B2), with the band further reduced as described in Section III-C.

B. PAM in Attenuating Media

Fig. 5 shows examples of PAM processing on both arrays simultaneously observing cavitation emissions—one array with a water path and the other with the attenuating phantom in the propagation path as in Fig. 2. Calibrated array data were processed with the RCB (upper row) and TEA (lower row) algorithms, with axial beam patterns through the map maxima shown in the far right column. The black line overlay in each PAM image denotes a 70%-amplitude contour. All images were produced by averaging PAM results from a full data set ($n = 28$ shots), with a fifth-order Butterworth bandpass filter between 3.6 and 9 MHz applied to all data prior to beamforming. A sound speed of 1490 m/s was used for all processing. The impact of sound speed uncertainty is addressed in Section III-E.

The effect of the phantom ($c_{\text{phan}} = 1505.8 \pm 0.5$ m/s at 6 MHz, $\alpha_{\text{phan,thru}} \sim 0.083 f^{0.86} \pm 0.002$ np/cm at 6 MHz, density $= 1030 \pm 10.3$ kg/m^3, plane wave transmission coefficient ~ 1.03) was to reduce the cavitation energy estimate by an order of magnitude, and to increase the axial half power beamwidth by 16.2% (RCB)–17.2% (TEA). Very similar map changes were seen with the RCB and TEA beamformers, although the latter starts from a place of coarser resolution and weaker sidelobe suppression even in the absence of attenuation. In both cases, the beamwidth dilation is associated with the low-pass filtering effect of the phantom: stronger attenuation and/or thicker media would further degrade the resolution of PAM images formed with broadband cavitation data. The "X" pattern visible in the TEA results is typical of a near-field beam pattern where emissions from a spatially concentrated source are received by a uniformly weighted array. Similar patterns are observed in the reciprocal case

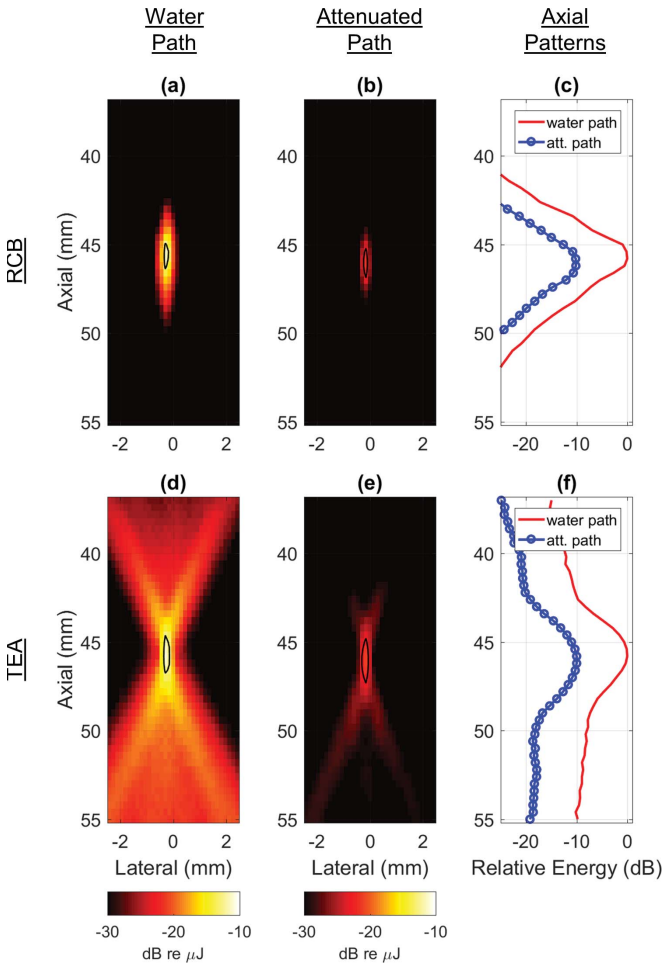

Fig. 5. PAM examples processed with RCB (top) and TEA (bottom). (a) and (d) Array without attenuating phantom in the propagation path. (b) and (e) Array with attenuating phantom in the path. (c) and (f) Axial beam patterns through map maxima. Results in (c) were normalized by the maximum value in (a), and the results in (f) were normalized the maximum value in (d). The black overlay on each colormap indicates a contour at 70% of the map maximum amplitude.

when a uniformly weighted array is used to transmit a focused field [36], [47]. The ability to minimize this diffraction effect is a clearly visible advantage of the array weights determined by the RCB algorithm.

C. Attenuation Estimation

The estimated total attenuation through the phantom is shown in Fig. 6 using the proposed cavitation-based method as applied to the same data set used to form the image in Fig. 5(b). In each of the six panels, results from the cavitation method are shown in red, while the blue curves are from the through-transmission method. The three columns indicate the SNR threshold used to set the upper cutoff frequency of the cavitation processing (10, 6, and 3 dB left to right). The green bar at the bottom of each panel indicates the frequency range over which the cavitation method was applied (with or without notch filtering), and dashed red lines indicate fit-based extensions of measurement data up to 9 MHz, which was the maximum frequency available for through-transmission test data. The cavitation-based results in the upper and lower rows were determined without and with a 100-kHz-wide notch filter, respectively, centered at 4 and 5 times the FUS drive frequency of 1.06 MHz.

In the frequency bands in which measurement data from the cavitation and through transmission methods overlapped, all processing variants yielded root-mean-square (rms) differences in total attenuation of less than 7% (1.1%–6.2% range, as shown in the lower left corner of each panel). Typically, the discrepancies were less than the calibration uncertainty of the reference hydrophone (±6%) used for substitution calibration of the needle hydrophone used for array characterization. To clarify, the absolute calibration level is not of concern for the cavitation-based method—only the uncertainty in spectrum shape over at least 2 MHz of bandwidth would influence the attenuation estimation results. Decreasing the SNR threshold increased the data bandwidth available for cavitation processing, which is seen to consistently improve precision (smaller error bars and normalized standard deviations listed in each panel). The use of the notch filter to remove scattering harmonics of the FUS drive frequency improved precision in all evaluation bands and accuracy in two of the three bands. Calculations made with notches extended up to the eighth FUS harmonic and widened up to 0.2 MHz (data not shown) showed no appreciable differences in attenuation estimation performance.

The cavitation-based estimates of attenuation show an apparent growth in frequency exponent as the SNR threshold is lowered (and processing bandwidth is increased). This is thought to be caused by small errors (<0.5 mm) in source localization, which may act to slightly decorrelate high-frequency array channel spectra when steering [phase term in (10)]. The resulting beamformed spectrum amplitude would errantly decrease with increasing frequency—a trend that would be interpreted by the fitting algorithm as an increased frequency exponent in the power law expression of attenuation.

The results in this section demonstrate the ability to estimate path attenuation using broadband cavitation spectra. These findings are carried into Section III-D, where the attenuation estimate is used to recover the energy of attenuation-free cavitation emissions.

D. PAM With Attenuation Compensation

The ability of the proposed compensation algorithm to estimate the cavitation source energy despite the presence of path attenuation is shown in Fig. 7 for the same data set shown in Fig. 5. The water path array measurement is shown in Fig. 7(a) and (d), the simultaneously acquired attenuated path array measurement is shown in Fig. 7(b) and (e), and the attenuation compensated processing of the data in Fig. 7(b) and (e) is displayed in Fig. 7(c) and (f). The color scale covers two orders of magnitude in order to visualize the attenuated maps without normalization. In the absence of calibration and processing errors, Fig. 7(a) and (c) should be identical, as should Fig. 7(d) and (f). The attenuation compensated results, processed with the 6-dB notch filtered

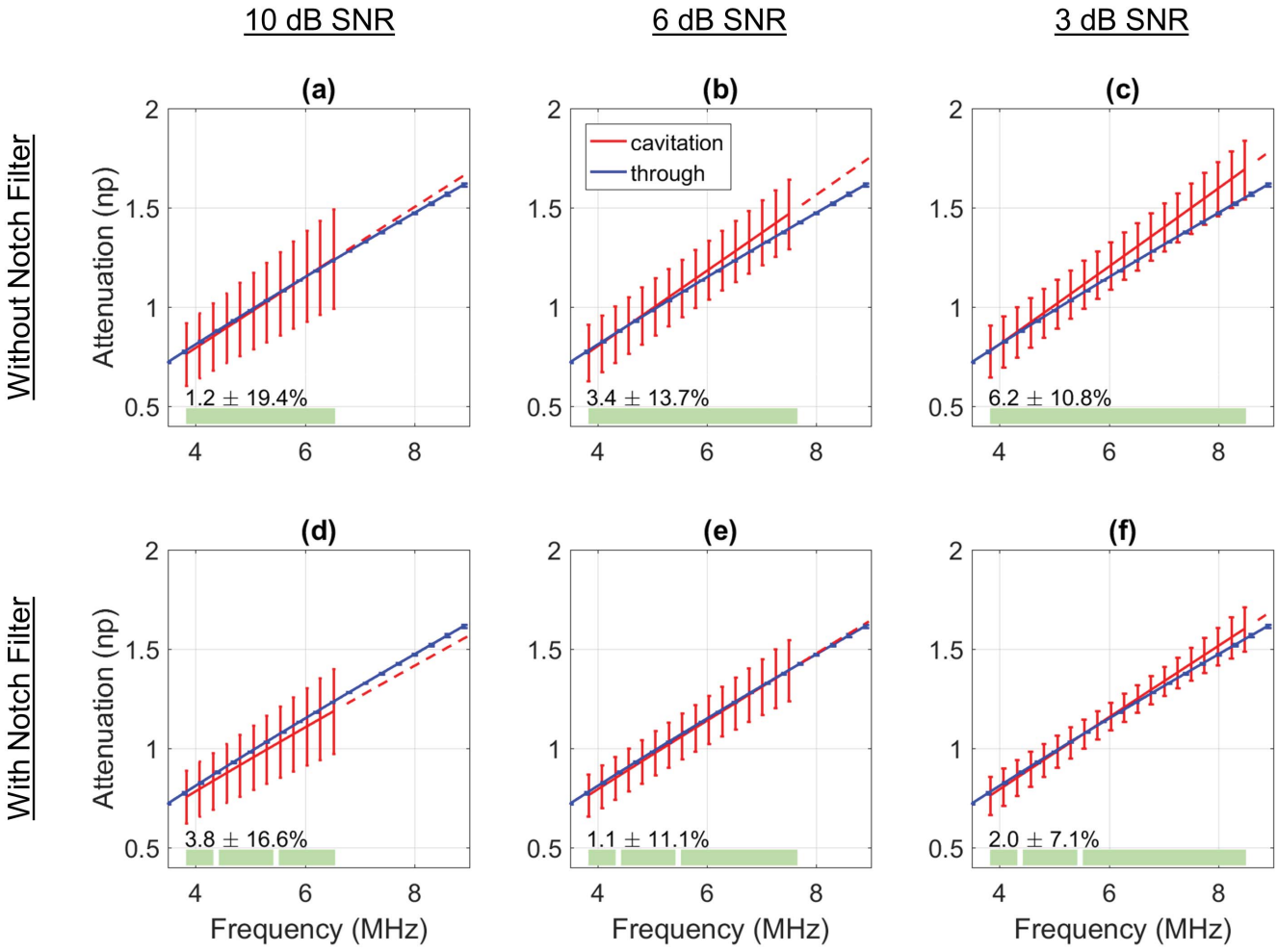

Fig. 6. Estimates of total path attenuation using cavitation and through-transmission methods. (a) and (d) 10-dB SNR cutoff. (b) and (e) 6-dB SNR cutoff. (c) and (f) 3-dB SNR cutoff. (a)–(c) Without notch filter. (d)–(f) With notch filter. The green bar indicates cavitation data evaluation band. Dashed lines indicate fit extensions to measurement results. Error bars indicate ±1 standard deviation. Numbers in the lower left of each panel indicate RMS and standard deviation of the difference between the two methods ($n = 28$), both normalized by the through-transmission result to give percentages.

attenuation estimate, qualitatively appear to be in good agreement with the water path (attenuation-free) maps, both in terms of peak energy and beam size. A slight axial elongation in Fig. 7(c) is visible, although this is occurring at a level approximately an order of magnitude below the map peak, and would therefore have negligible impact on source localization. Noise amplification in the attenuation compensation process appears to be minimal because the images do not exhibit substantial background elevation [38].

Attenuation compensation processing statistics for the full experiment data set ($n = 28$) are presented in Fig. 8 for results obtained with TEA and RCB PAM algorithms, both using the 6-dB SNR notch filtered attenuation estimate. All input data (water path, attenuated path, compensated) were conditioned with an identical 3.6–9-MHz bandpass filter so that the processing statistics could be equitably compared.

The peak energy estimates in Fig. 8(a) show close agreement between compensated and water path data for the TEA (5.9%) and RCB (2.9%) algorithms, where the values in parenthesis indicate percentage difference of mean values. All estimation errors are well below the reference hydrophone calibration error (12.5% for energy calculation based on the square of pressure).

Lateral half-amplitude beamwidth results in Fig. 8(b) indicated close agreement between water path and compensated data sets (TEA 2.9%, RCB 3.7%), although the initial effect of attenuation was small to begin with (8.6, 3.6% widening for TEA, RCB, respectively). For perspective, the mean RCB lateral widths (0.27–0.29 mm) were nearly identical to the 0.3-mm inner diameter of the tubing where UCA was flowing. As such it appears that the primary driver of lateral beamwidth was the physical configuration of the experiment rather than path losses.

The UCA-filled tube used in these experiments presented a circular cross section to the array in the xz (lateral-depth) imaging plane. If all microbubbles responded equally to the incident field, 90% of the scattering amplitude would come from the central 80% of the tube (0.24 mm wide) based on lateral integration of the circular cross section. This is because the central part of the tube contains more scatterers

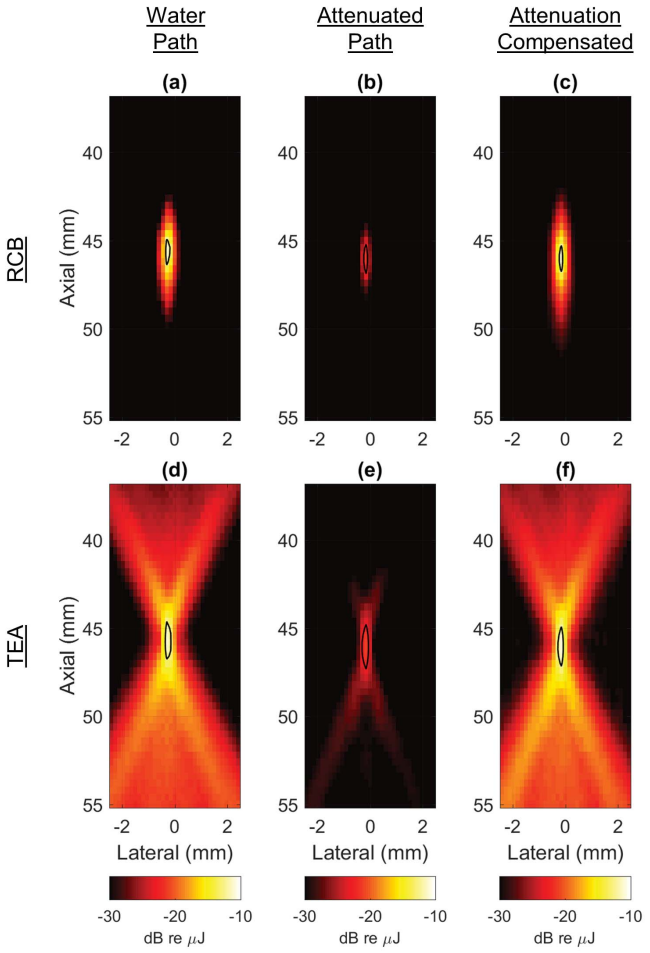

Fig. 7. PAM attenuation compensation examples processed with RCB (top) and TEA (bottom) beamformers. (a) and (d) Water path array. (b) and (e) Array with attenuating phantom in the path. (c) and (f) Attenuation compensated maps using data from (b) and (e). The black overlay on each colormap indicates a contour at 70% of the map maximum amplitude.

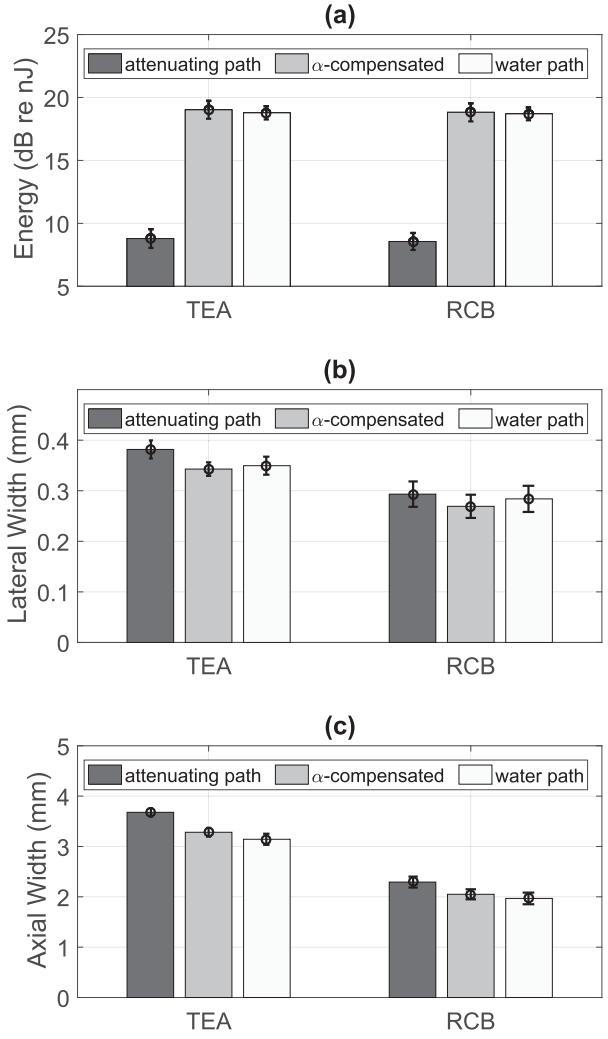

Fig. 8. Summary statistics quantifying attenuation impact and compensation on (a) peak map energy, (b) lateral half power full beamwidth, and (c) axial half power full beamwidth. In each panel, the three groups of bars were calculated for TEA and RCB beamforming algorithms. In each bar group, the bar height indicates ensemble mean, and the error bars indicates one standard deviation ($n = 28$).

per unit lateral width than does the peripheral area (extremes at $+/- x$). Similarly, 90% of the scattered *energy* would come from the central 73% (0.22 mm wide). If sources within the full diameter of tubing do not contribute evenly to the emitted field, but instead contribute in this edge-tapered fashion, then the imaged cavitation width may be narrower than the tube diameter if the point spread function (PSF) allows.

For a uniformly weighted array aperture (as in TEA beamforming), the lateral half power full width is 0.23 mm at 7 MHz and a depth of 45 mm [34, eq. (4)]. For RCB, the array weights are typically end-amplified, resulting in a narrower PSF. Taken together, these results appear to support the numerical values displayed in Fig. 8.

The axial beamwidth changes after attenuation compensation are similar to those seen with lateral beamwidth, with similarly good agreement between water path and compensated data sets (TEA 4.5, RCB 4.1%). For context on the absolute sizes, the mean axial half power widths would be expected for a uniformly weighted L11-4v array responding at 4.8 and 7.7 MHz for TEA and RCB, respectively [34, eq.(5)]. This illustrates how RCB may manipulate array weights to reduce beamwidth when aperture and bandwidth are fixed.

Both beamformers were biased toward lower frequencies as a consequence of FUS harmonic scattering contributions below 5 MHz. For example, the rms water path array response was 73% higher in the 4–6 MHz band than did in the 6–8 MHz band. Therefore, the benefit of response spectrum rebalancing by enhancing high frequencies (both through calibration and attenuation compensation) will be limited in terms of resolution in the present data sets unless further signal conditioning (i.e., high-pass filtering) is performed.

Finally, a paired-t test (alpha $= 0.05$) indicated a lack of statistical significance ($p = 0.31$) for the differences between the water path and attenuation compensated energies. As a whole, the results from this section demonstrate the ability of the proposed procedures to accurately estimate the cavitation energy that would have been observed in a loss-free path.

E. Sound Speed Uncertainty

All processing performed on the data described above used an identical sound speed for both array measurements. The impact of sound speed uncertainty on the attenuation processing steps, from "source" localization through attenuation compensation, was quantified by varying the presumed sound speed over the range $[c_0, c_0 \pm 20, 40]$ m/s, where $c_0 = 1490$ m/s was the value used in the prior sections, and was approximately the mean of the tank water (1482.4, seen by the water path array) and the path average of the phantom and water (1505.8, seen by the "attenuated" array). The range of speeds used here spans well beyond the values for constituent materials. Looking ahead to simulation of potential clinical therapeutic applications, the estimated path average speeds do not need to cover the extremes (e.g., slowest fats in the propagation path for a liver treatment) in order to represent a relevant treatment scenario through a mix of tissue compositions. The evaluation process began by running the PAM beamformers, estimating a source position, and using those estimates in the subsequent attenuation estimation and compensation processes. A 6-dB SNR threshold with notch filtering was used for the latter two steps.

Fig. 9 shows summary statistics describing the impact of sound speed uncertainty on cavitation source ranging, path attenuation estimation, and energy recovery. All displayed results were found using the RCB PAM algorithm, but similar results were found using TEA PAM (data not shown). In Fig. 9(a), the axial distance where the peak PAM energy was identified is shown as a function of presumed sound speed for the water path reference and uncompensated attenuated arrays. Bar heights are mean values over the full data set ($n = 28$ shots), and no standard deviation error bars are shown, as they are $<1\%$ of the mean.

A key result is that the estimated axial range (z_{est}) shifts approximately linearly with the ratio of presumed (c_{est}) and actual sound speed, but with inverse proportion: $z_{\text{est}} \sim z_0 \times (c_0/c_{\text{est}})$. That the cavitation source would be mapped closer to the array when an errantly high sound speed is used is opposite to how the same sound speed error would impact range estimation in a conventional pulse-echo or B-mode system. This feature of passive mapping results from the use of relative response delays between elements, rather than absolute time of flight to estimate source position [5].

Following the trend of axial distance, the attenuation estimates in Fig. 9(b) decrease linearly as the presumed sound speed is increased. The attenuation changes appear to be primarily in the form of a linear scaling ((11b), which contains distance information) without a significant change in frequency exponent ($0.90 \pm 1.3\%$).

Normalizing the total attenuation by the estimated range gives an estimated path average attenuation coefficient which is nearly independent of presumed sound speed: 0.26 np/cm $\pm$ 0.6% at 6 MHz. It is important to reiterate that neither the beamformers nor the attenuation estimator receive any prior knowledge of the constituent materials or geometries in the propagation path between cavitation event and array. Therefore, when attenuation is estimated from the beamformed spectrum, it is the path total value by necessity. When normalized by estimated distance (array to point in the image), the estimated attenuation is a path-average value. In both cases, the attenuation values are specific to the location of the cavitation events used for the computation. In a clinical scenario, we would expect several attenuation estimates to be calculated at different locations within a region of interest, with the map energies compensated by the locally determined attenuation estimates.

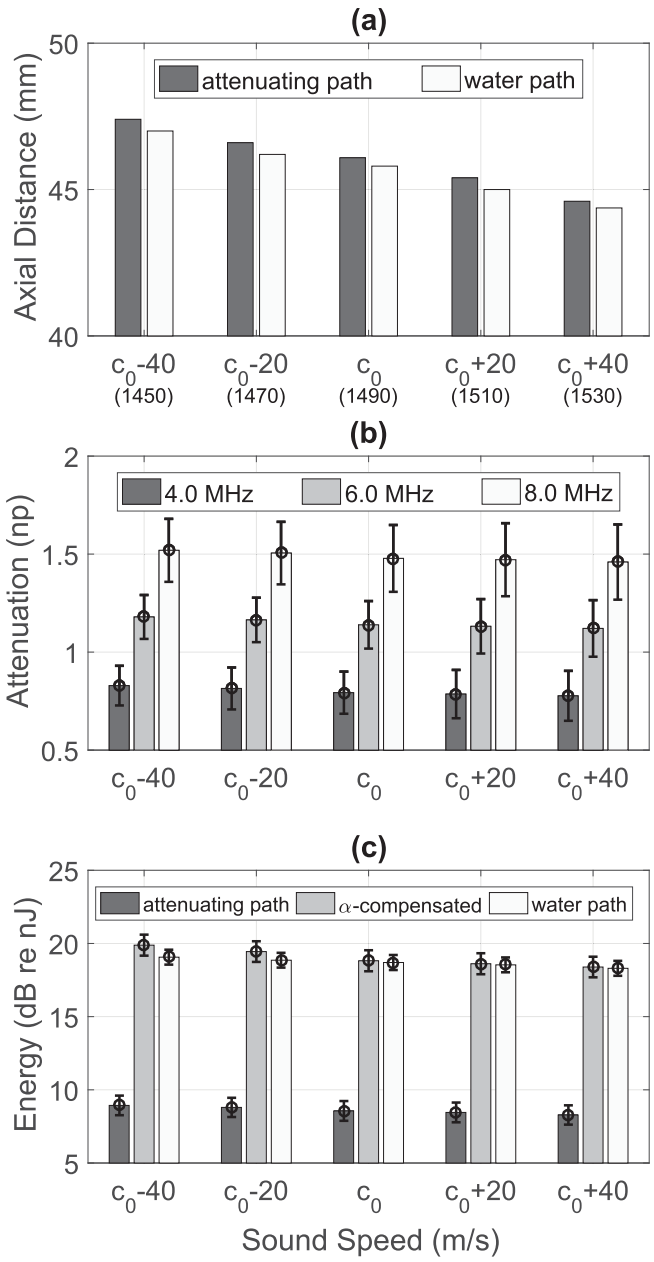

Fig. 9. Summary results of the target range, attenuation estimation, and energy calculation processes for a range of presumed path average sound speeds. (a) Axial distance to the location of PAM peak energy, determined for the two arrays simultaneously monitoring cavitation. Parenthetical numbers below the abscissa indicate the sound speeds used in the calculations. (b) Attenuation estimates at three frequencies. (c) Peak energy estimates. In each bar group, the bar height indicates ensemble mean, and the error bars indicates one standard deviation ($n = 28$). The RCB PAM algorithm was used for all calculations.

The peak cavitation map energies in Fig. 9(c) show the strongest sensitivity to sound speed. Referring back to (1) and (2), the water path array results should scale approximately as

$$E_{\text{est}} \sim E_{\text{act}} \times (c_{\text{act}}/c_{\text{est}})^3 \tag{14}$$

where E_{act} is the energy calculated using the actual path averaged sound speed c_{act}. The cubic dependence arises because the energy estimation process is quadratic in estimated range from source to array [which scales as $(c_{\text{act}}/c_{\text{est}})$ according to Fig. 9(a)] and also involves scaling by sound speed in the denominator of (1). Note that for all energy calculations, density was held fixed at 1000 kg/m^3. For the range of sound speeds examined, (14) suggests error bounds of $+6.8\%$ to -9.1% from slowest to fastest speeds, with the asymmetry resulting from the water path speed being 1482 m/s—slightly less than the center value of the evaluated range (1490 m/s). The peak energy estimation errors agree well with the data range of $+8.8\%$ to -9.7%.

The attenuation compensated energies are more sensitive because the sound speed error also appears in the total attenuation estimate, with the range and attenuation errors biased in the same direction. In this case, peak energy scaling includes an attenuation correction of $\exp(2\bar{\alpha}_{\text{est,tot}})$, where the estimated total attenuation scales with $c_{\text{act}}/c_{\text{est}}$ according to Fig. 9(b). Keeping the first two series expansion terms of the exponential, the energy scaling with attenuation included is approximately

$$E_{\text{est},\alpha_{\text{est}}} \sim E_{\text{act},\alpha_{\text{act}}} \times (c_{\text{act}}/c_{\text{est}})^3 \times (1 + 2\bar{\alpha}_{\text{act,tot}}(c_{\text{act}}/c_{\text{est}} - 1)) \tag{15}$$

which is evaluated by integrating over the frequency band used in PAM processing (Section II-F). When evaluated using $\bar{\alpha}_{\text{act,tot}}$ as determined from the through-transmission measurements, (15) suggests error bounds of $+23.7$ to -8.9%, similar to the data range of $+27.7\%$ to -9.3%.

While the peak energy calculations proved to be most sensitive of the metrics considered, the estimation errors for the specified range of speeds are small compared to the potential errors when an incorrect attenuation is assumed. For example, using the on-axis source distance ($\sim$46 mm) and processing band (3.6–9 MHz) employed for the processing leading to Fig. 9, the choice of 0.06 np/cm/MHz if the true path average is 0.072 leads to a factor of two error in energy estimation even if the sound speed is perfectly known. The same size error would be found when using a fixed linear term (0.06 np/cm/MHz) but assuming a frequency exponent of 1 when the true exponent is 1.07.

IV. Discussion

A technique for attenuation estimation based on broadband cavitation spectra has been presented. The proposed technique is unilateral (not a through-transmission method), does not require an extracorporeal reflector, and is self-referencing, so that probe handling and implementation could be similar to conventional hand-held diagnostic ultrasound. Relative to backscatter methods for attenuation estimation, the impact of speckle scattering should be minimal since the signals being operated upon consist of forward (one-way) propagating emissions from an internally generated broadband source. However, unlike B-mode-based methods, the proposed technique requires broadband cavitation noise to be present and detectible within the available measurement SNR. Therefore, it is best suited to applications in which inertial cavitation is desired [48]–[50].

The methods presented here were initially intended to support cavitation-mediated drug delivery—an emerging field of therapeutic ultrasound where previous studies have shown a relationship between total cavitation activity and therapeutic effect. Existing cavitation monitoring routines do not account for attenuation and would be strongly biased within a patient and between patients. This bias could be removed using the proposed attenuation estimation and compensation techniques, and could therefore enable consistent evaluation of total cavitation and its relationship to therapeutic effects.

Beyond drug delivery, there are a variety of other therapeutic ultrasound applications (blood–brain barrier opening, endothelium damage, ablation) whose efficacy thresholds have been quantified in terms of cavitation activity. For the latter, the ability to estimate cavitation energy has been shown to enable substantially improved temperature elevation estimates provided that attenuation is properly estimated [46].

Since the attenuation estimates are produced as frequency-dependent function fits, they could be used to inform HIFU drive parameters (if the transmit and receive systems have overlapping propagation paths) by extending the fits down to the HIFU drive frequency, as well as to intermediate frequencies produced by nonlinear propagation for assessment of heating rate. Any such projection is done with modest risk depending on the relative values of the HIFU drive and attenuation evaluation frequencies, but this would still appear to be a better informed patient-specific estimate than what would be achieved by assuming average literature-based values for constituent tissues.

The present work employed relatively short FUS pulses that were sufficient for demonstrating the proposed processing techniques, but these exposures differ substantially from the long or continuous transmissions used in many emerging or current clinical procedures as cited above. However, longer pulse lengths are expected to improve the performance of the attenuation estimation technique by providing more events to process when forming the received spectrum. PAM and other passive mapping methods do not use any timing information from the FUS transmissions, nor do they involve any high-frequency transmission (as with active or B-mode methods), so the process of cavitation event localization can occur at any point during the FUS transmission. Therefore, neither the localization nor spectrum characterization aspects of the proposed attenuation estimation method should be adversely impacted by increased FUS transmission times.

While the experiment apparatus was useful for evaluating the concepts proposed in this paper, the spatial extent of cavitation activity was constrained by the tube flow arrangement, the propagation media (water and phantom) had simple geometries and similar sound speeds, and the cavitation itself was a mix of harmonic and broadband determined by the FUS

signal and the flowing UCA. Regarding the latter, while clinical applications may proceed with or without micrometer-scale UCAs or seeding particles, broadband emissions from inertially collapsing bubbles should be functionally the same for the purposes of attenuation processing regardless of bubble origin, i.e., whether the nuclei were natural or exogenous. Still, the effectiveness and robustness of the presented processing techniques under more clinically representative conditions (i.e., layered and curved constituent materials, spatially distributed cavitation sources) are the subjects of ongoing research.

Energy recovery processing presumes linear propagation between the cavitation source(s) and the receive array. Prior research has found this to be a valid assumption even in the absence of thermoviscous attenuation [51]. If measurements were made in soft tissue infused with distributed contrast agents, total path attenuation may be increased relative to that of the native tissue matrix as a result of nonlinear scattering. The effect would be most pronounced at harmonics of the FUS drive frequency, but these frequencies are not used in the attenuation estimation process. Moreover, any broadband spectrum modification due to the presence of distributed UCAs would indicate the actual and therefore relevant path attenuation at the time of treatment. It may be that observations of broadband cavitation spectral trends over the course of a treatment could provide a measure of the distribution and concentration of UCAs, especially if a reference data set was acquired prior to UCA infusion.

Sound speed uncertainty analysis revealed source ranging errors in proportion to the ratio of the actual and presumed path averaged propagation speeds. The maximum observed axial shift in PAM energy peak was approximately 1.6 mm, which is on the order of 3/4 the RCB PAM axial beamwidth [see Fig. 8(c)]. The range shifts and axial beamwidths will increase linearly and quadratically with larger source distances, respectively, so this effect is not envisioned to be of major consequence to clinical implementation of PAM.

The processing steps described in this paper are fairly simple, but would still add to the computational burden of any real time monitoring system. As previously pointed out for diffraction processing [38], faster algorithmic implementation will be possible through the use of frequency domain beamforming [9], for which retained data volumes are smaller and multiple inversions (time to frequency to time) of element data are unnecessary. All of these approaches may be further accelerated through the use of graphical processing units [9], [52].

The accuracy of the cavitation-based method for attenuation estimation is contingent upon careful array calibration. As indicated by the power law fits to the uncalibrated data in Fig. 1, if the combined element sensitivities and diffraction terms are left uncorrected, a substantial error would result. Numerically, the uncalibrated response slope would have increased the estimated total phantom attenuation by approximately 75%. Calibration, including diffraction corrections over the full range of cavitation monitoring locations, can be extremely time-consuming even when using the streamlined methods and reduced measurement ranges presented in Section II-B. Moreover, while the proposed method provides a total attenuation estimate over the path between cavitation site and the monitoring array, there may be instances where it would be desirable to localize changes in attenuation during treatment. An approach for attenuation estimation with enhanced localization capability and relaxed requirements for calibration is the subject of ongoing research.

V. Conclusion

The results of this study quantified the impact of attenuation on PAM-based estimates of cavitation energy, showing that order of magnitude effects are possible in propagation paths as short as 4 cm. Correction of both diffraction and attenuation effects will be essential for quantitative comparison of PAM data from different patients with different target depths or if monitored with different arrays. In concert with PAM, the proposed techniques for attenuation estimation and cavitation energy recovery are intended to improve the safety and efficacy of therapeutic ultrasound procedures, especially those whose bioeffects are tied to a specific level of cavitation. If in a given treatment scenario, a certain amount of cavitation was expected but not observed, it may not initially be clear whether the discrepancy was related to FUS field strength, the population of cavitation nuclei, or simply that the observations were hindered by incorrectly estimated propagation conditions. The techniques proposed herein may help resolve these challenges.

The proposed techniques may also have significant implications for diagnostic ultrasound applications. For example, the broadband attenuation estimates described here may be used to enhance the performance of existing methods for B-mode image compensation [53], [54], or scatterer size estimation [55]. In the context of ablative treatments, attenuation estimates may also provide corroboration or supporting data for elastography techniques [56] or more conventional quantitative ultrasound assessments.

Acknowledgment

The authors would like to thank Dr. E. Lyka, Dr. D. Elbes, Dr. M. Gyongy, and C. Paverd for their helpful discussions.

References

[1] W. J. Elias *et al.*, "A randomized trial of focused ultrasound thalamotomy for essential tremor," *New England J. Med.*, vol. 375, no. 8, pp. 730–739, Aug. 2016.

[2] A. Carpentier *et al.*, "Clinical trial of blood-brain barrier disruption by pulsed ultrasound," *Sci. Transl. Med.*, vol. 8, no. 343, p. 343re2, Jun. 2016.

[3] P. C. Lyon *et al.*, "Clinical trial protocol for TARDOX: A phase I study to investigate the feasibility of targeted release of lyso-thermosensitive liposomal doxorubicin (ThermoDox) using focused ultrasound in patients with liver tumours," *J. Therapeutic Ultrasound*, vol. 5, no. 1, p. 28, Nov. 2017.

[4] G. Dimcevski *et al.*, "A human clinical trial using ultrasound and microbubbles to enhance gemcitabine treatment of inoperable pancreatic cancer," *J. Controlled Release*, vol. 243, pp. 172–181, Dec. 2016.

[5] M. Gyongy, M. Arora, J. A. Noble, and C.-C. Coussios, "Use of passive arrays for characterization and mapping of cavitation activity during HIFU exposure," in *Proc. IEEE Ultrason. Symp.*, Nov. 2008, pp. 871–874.

[6] V. A. Salgaonkar, S. Datta, C. K. Holland, and T. D. Mast, "Passive cavitation imaging with ultrasound arrays," *J. Acoust. Soc. Amer.*, vol. 126, no. 6, pp. 3071–3083, Dec. 2009.

[7] M. Gyöngy and C.-C. Coussios, "Passive spatial mapping of inertial cavitation during HIFU exposure," *IEEE Trans. Biomed. Eng.*, vol. 57, no. 1, pp. 48–56, Jan. 2010.

[8] C. Coviello *et al.*, "Passive acoustic mapping utilizing optimal beamforming in ultrasound therapy monitoring," *J. Acoust. Soc. Amer.*, vol. 137, no. 5, pp. 2573–2585, May 2015.

[9] K. J. Haworth, K. B. Bader, K. T. Rich, C. K. Holland, and T. D. Mast, "Quantitative frequency-domain passive cavitation imaging," *IEEE Trans. Ultrason., Ferroelectr., Freq. Control*, vol. 64, no. 1, pp. 177–191, Jan. 2017.

[10] C. D. Arvanitis, C. Crake, N. McDannold, and G. T. Clement, "Passive acoustic mapping with the angular spectrum method," *IEEE Trans. Med. Imag.*, vol. 36, no. 4, pp. 983–993, Apr. 2017.

[11] J. Gateau, J.-F. Aubry, M. Pernot, M. Fink, and M. Tanter, "Combined passive detection and ultrafast active imaging of cavitation events induced by short pulses of high-intensity ultrasound," *IEEE Trans. Ultrason., Ferroelectr., Freq. Control*, vol. 58, no. 3, pp. 517–532, Mar. 2011.

[12] T. Ding, S. Zhang, Q. Fu, Z. Xu, and M. Wan, "Ultrasound line-by-line scanning method of spatial–temporal active cavitation mapping for high-intensity focused ultrasound," *Ultrasonics*, vol. 54, no. 1, pp. 147–155, Jan. 2014.

[13] T. Li, T. D. Khokhlova, O. A. Sapozhnikov, M. O'Donnell, and J. H. Hwang, "A new active cavitation mapping technique for pulsed HIFU applications-bubble Doppler," *IEEE Trans. Ultrason., Ferroelectr., Freq. Control*, vol. 61, no. 10, pp. 1698–1708, Oct. 2014.

[14] N. McDannold, N. Vykhodtseva, and K. Hynynen, "Targeted disruption of the blood–brain barrier with focused ultrasound: Association with cavitation activity," *Phys. Med. Biol.*, vol. 51, no. 4, pp. 793–807, Feb. 2006.

[15] C. D. Arvanitis, M. S. Livingstone, and N. McDannold, "Combined ultrasound and MR imaging to guide focused ultrasound therapies in the brain," *Phys. Med. Biol.*, vol. 58, no. 14, pp. 4749–4761, Jul. 2013.

[16] C. R. Jensen, R. W. Ritchie, M. Gyöngy, J. R. T. Collin, T. Leslie, and C.-C. Coussios, "Spatiotemporal monitoring of high-intensity focused ultrasound therapy with passive acoustic mapping," *Radiology*, vol. 262, no. 1, pp. 252–261, Jan. 2012.

[17] J. H. Hwang, J. Tu, A. A. Brayman, T. J. Matula, and L. A. Crum, "Correlation between inertial cavitation dose and endothelial cell damage *in vivo*," *Ultrasound Med. Biol.*, vol. 32, no. 10, pp. 1611–1619, Oct. 2006.

[18] G. R. ter Haar, "Ultrasound focal beam surgery," *Ultrasound Med. Biol.*, vol. 21, no. 9, pp. 1089–1100, 1995.

[19] R. O. Illing *et al.*, "The safety and feasibility of extracorporeal high-intensity focused ultrasound (HIFU) for the treatment of liver and kidney tumours in a Western population," *Brit. J. Cancer*, vol. 93, no. 8, pp. 890–895, Oct. 2005.

[20] N. Ellens and K. Hynynen, "Frequency considerations for deep ablation with high-intensity focused ultrasound: A simulation study," *Med. Phys.*, vol. 42, no. 8, pp. 4896–4910, Aug. 2015.

[21] J. C. Bamber and C. R. Hill, "Ultrasonic attenuation and propagation speed in mammalian tissues as a function of temperature," *Ultrasound Med. Biol.*, vol. 5, no. 2, pp. 149–157, Jan. 1979.

[22] N. L. Bush, I. Rivens, G. R. ter Haar, and J. C. Bamber, "Acoustic properties of lesions generated with an ultrasound therapy system," *Ultrasound Med. Biol.*, vol. 19, no. 9, pp. 789–801, 1993.

[23] M. R. Gertner, B. C. Wilson, and M. D. Sherar, "Ultrasound properties of liver tissue during heating," *Ultrasound Med. Biol.*, vol. 23, no. 9, pp. 1395–1403, 1997.

[24] V. Zderic, A. Keshavarzi, M. A. Andrew, S. Vaezy, and R. W. Martin, "Attenuation of porcine tissues *in vivo* after high-intensity ultrasound treatment," *Ultrasound Med. Biol.*, vol. 30, no. 1, pp. 61–66, Jan. 2004.

[25] M. Fink, F. Hottier, and J. F. Cardoso, "Ultrasonic signal processing for *in vivo* attenuation measurement: Short time Fourier analysis," *Ultrason. Imag.*, vol. 5, no. 2, pp. 117–135, 1983.

[26] K. J. Parker, R. M. Lerner, and R. C. Waag, "Comparison of techniques for *in vivo* attenuation measurements," *IEEE Trans. Biomed. Eng.*, vol. BME-35, no. 12, pp. 1064–1068, Dec. 1988.

[27] L. X. Yao, J. A. Zagzebski, and E. L. Madsen, "Backscatter coefficient measurements using a reference phantom to extract depth-dependent instrumentation factors," *Ultrason. Imag.*, vol. 12, no. 1, pp. 58–70, 1990.

[28] S. L. Baldwin, M. R. Holland, D. E. Sosnovik, and J. G. Miller, "Effects of region-of-interest length on estimates of myocardial ultrasonic attenuation and backscatter," *Med. Phys.*, vol. 32, no. 2, pp. 418–426, Feb. 2005.

[29] N. Rubert and T. Varghese, "Scatterer number density considerations in reference phantom based attenuation estimation," *Ultrasound Med. Biol.*, vol. 40, no. 7, pp. 1680–1696, Jul. 2014.

[30] E. Omari, H. Lee, and T. Varghese, "Theoretical and phantom based investigation of the impact of sound speed and backscatter variations on attenuation slope estimation," *Ultrasonics*, vol. 51, no. 6, pp. 758–767, Aug. 2011.

[31] M. D. Gray and P. H. Rogers, "*In vivo* ultrasonic attenuation in cetacean soft tissues," *J. Acoust. Soc. Amer.*, vol. 141, no. 2, pp. EL83–EL88, Feb. 2017.

[32] S.-W. Huang and P.-C. Li, "Ultrasonic computed tomography reconstruction of the attenuation coefficient using a linear array," *IEEE Trans. Ultrason., Ferroelectr., Freq. Control*, vol. 52, no. 11, pp. 2011–2022, Nov. 2005.

[33] C. Li, N. Duric, and L. Huang, "Comparison of ultrasound attenuation tomography methods for breast imaging," *Proc. SPIE*, vol. 6920, p. 692015, Mar. 2008.

[34] M. Gyöngy and C.-C. Coussios, "Passive cavitation mapping for localization and tracking of bubble dynamics," *J. Acoust. Soc. Amer.*, vol. 128, no. 4, p. EL175, Oct. 2010.

[35] J. Li, P. Stoica, and Z. Wang, "On robust Capon beamforming and diagonal loading," *IEEE Trans. Signal Process.*, vol. 51, no. 7, pp. 1702–1715, Jul. 2003.

[36] D. A. Guenther and W. F. Walker, "A method for accurate *in silico* modeling of ultrasound transducer arrays," *Ultrasonics*, vol. 49, nos. 4–5, pp. 404–412, May 2009.

[37] P. Stepanishen, "Pulsed transmit/receive response of ultrasonic piezoelectric transducers," *J. Acoust. Soc. Amer.*, vol. 69, no. 6, pp. 1815–1827, 1981.

[38] M. D. Gray, E. Lyka, and C.-C. Coussios, "Diffraction effects and compensation in passive acoustic mapping," *IEEE Trans. Ultrason., Ferroelectr., Freq. Control*, vol. 65, no. 2, pp. 258–268, Feb. 2018.

[39] W. Marczak, "Water as a standard in the measurements of speed of sound in liquids," *J. Acoust. Soc. Amer.*, vol. 102, no. 5, pp. 2776–2779, Nov. 1997.

[40] K. V. Ramnarine, T. Anderson, and P. R. Hoskins, "Construction and geometric stability of physiological flow rate wall-less stenosis phantoms," *Ultrasound Med. Biol.*, vol. 27, pp. 245–250, Feb. 2001.

[41] E. L. Madsen, J. A. Zagzebski, and G. R. Frank, "Oil-in-gelatin dispersions for use as ultrasonically tissue-mimicking materials," *Ultrasound Med. Biol.*, vol. 8, no. 3, pp. 277–287, 1982.

[42] T. G. Leighton, *The Acoustic Bubble*. London, U.K.: Academic, 1994.

[43] C. D. Arvanitis, M. Bazan-Peregrino, B. Rifai, L. W. Seymour, and C.-C. Coussios, "Cavitation-enhanced extravasation for drug delivery," *Ultrasound Med. Biol.*, vol. 37, no. 11, pp. 1838–1852, Nov. 2011.

[44] D. E. Kruse and K. W. Ferrara, "A new imaging strategy using wideband transient response of ultrasound contrast agents," *IEEE Trans. Ultrason., Ferroelectr., Freq. Control*, vol. 52, no. 8, pp. 1320–1329, Aug. 2005.

[45] I. Tzanakis, G. S. B. Lebon, D. G. Eskin, and K. A. Pericleous, "Characterizing the cavitation development and acoustic spectrum in various liquids," *Ultrason. Sonochem.*, vol. 34, pp. 651–662, Jan. 2017.

[46] C. R. Jensen, R. O. Cleveland, and C.-C. Coussios, "Real-time temperature estimation and monitoring of HIFU ablation through a combined modeling and passive acoustic mapping approach," *Phys. Med. Biol.*, vol. 58, no. 17, pp. 5833–5850, 2013.

[47] S. A. Ilyin, P. V. Yuldashev, V. A. Khokhlova, L. R. Gavrilov, P. B. Rosnitskiy, and O. A. Sapozhnikov, "Analytical method for evaluating the quality of acoustic fields radiated by a multielement therapeutic array with electronic focus steering," *Acoust. Phys.*, vol. 61, no. 1, pp. 52–59, 2015.

[48] T. D. Khokhlova, M. S. Canney, V. A. Khokhlova, O. A. Sapozhnikov, L. A. Crum, and M. R. Bailey, "Controlled tissue emulsification produced by high intensity focused ultrasound shock waves and millisecond boiling," *J. Acoust. Soc. Amer.*, vol. 130, pp. 3498–3510, May 2011.

[49] B. Petit *et al.*, "Sonothrombolysis: The contribution of stable and inertial cavitation to clot lysis," *Ultrasound Med. Biol.*, vol. 41, no. 5, pp. 1402–1410, May 2015.

[50] R. Myers *et al.*, "Polymeric cups for cavitation-mediated delivery of oncolytic vaccinia virus," *Mol. Therapy*, vol. 24, no. 9, pp. 1627–1633, Sep. 2016.

[51] J. R. T. Collin and C.-C. Coussios, "Quantitative observations of cavitation activity in a viscoelastic medium," *J. Acoust. Soc. Amer.*, vol. 130, no. 5, pp. 3289–3296, Nov. 2011.

[52] E. Lyka, C. Coviello, R. Kozick, and C.-C. Coussios, "Sum-of-harmonics method for improved narrowband and broadband signal quantification during passive monitoring of ultrasound therapies," *J. Acoust. Soc. Amer.*, vol. 140, no. 1, pp. 741–754, Jul. 2016.
[53] D. I. Hughes and F. A. Duck, "Automatic attenuation compensation for ultrasonic imaging," *Ultrasound Med. Biol.*, vol. 23, no. 5, pp. 651–664, 1997.
[54] G. Treece, R. Prager, and A. Gee, "Ultrasound attenuation measurement in the presence of scatterer variation for reduction of shadowing and enhancement," *IEEE Trans. Ultrason., Ferroelectr., Freq. Control*, vol. 52, no. 12, pp. 2346–2360, Dec. 2005.
[55] M. L. Oelze and W. D. O'Brien, Jr., "Frequency-dependent attenuation-compensation functions for ultrasonic signals backscattered from random media," *J. Acoust. Soc. Amer.*, vol. 111, no. 5, pp. 2308–2319, May 2002.
[56] E. S. Ebbini and G. R. Ter Haar, "Ultrasound-guided therapeutic focused ultrasound: Current status and future directions," *Int. J. Hyperthermia*, vol. 31, no. 2, pp. 77–89, Mar. 2015.

Michael D. Gray received the B.S. degree in mechanical engineering from Tufts University, Medford, MA, USA, in 1990, and the M.S. and Ph.D. degrees in mechanical engineering from the Georgia Institute of Technology, Atlanta, GA, USA, in 1992 and 2015, respectively.

From 1992 to 2015, he was a Research Engineer at the Georgia Institute of Technology. Since 2015, he has been a Senior Research Fellow with the Biomedical Ultrasonics, Biotherapy and Biopharmaceuticals Laboratory, Institute of Biomedical Engineering, University of Oxford, Oxford, U.K. His research interests include the use of sound, magnetism and light for targeted drug delivery, clinical translation of cavitation monitoring techniques, and hearing in marine animals.

Constantin C. Coussios received the B.A., M.Eng., M.A., and Ph.D. degrees from the University of Cambridge, Cambridge, U.K., in 1977, 1998, 2000, and 2002, respectively.

He is currently the Director of the Oxford Institute of Biomedical Engineering, a Statutory Professor of biomedical engineering, and the Head of the Biomedical Ultrasonics, Biotherapy and Biopharmaceuticals Laboratory with the University of Oxford, Oxford, U.K. He is also the Co-Founder and a Director of two biomedical technology companies: OrganOx Ltd., Oxford, and OxSonics, Ltd.

Dr. Coussios was elected fellow of the Acoustical Society of America (ASA) in 2009. He was a recipient of the F.V. Hunt Post-Doctoral Fellowship of the ASA from 2002 to 2003, ASA's 2012 Bruce Lindsay Award, and the ISTU Frederic Lizzi Award in 2012. He served as Secretary General of the International Society in Therapeutic Ultrasound from 2006 to 2010. In 2017, he was awarded the Silver Medal by the U.K.'s Royal Academy of Engineering.